A comparative study of the correlation between diffusion length of charge carriers and the performance of $CsSnGeI_3$ perovskite solar cells

Ali K. Al-Mousoi[1], Mustafa K. A. Mohammed[2,*], Sinan Q. Salih[3], Rahul Pandey[4], Jaya Madan[4], Davoud Dastan[5], Erdi Akman[6], AbdulRahman A. Alsewari[7], Zaher Mundher Yaseen[8]

[1]Department of Radiology and Ultrasonography Techniques, College of Medical Techniques, Al-Farahidi University, Baghdad 10011, Iraq

[2] Radiological Techniques Department, Al-Mustaqbal University College, 51001 Hillah, Babylon, Iraq

[3]Department of Communication Technology Engineering, College of Information Technology, Imam Ja'afar Al-Sadiq University, Baghdad 10011, Iraq

[4]VLSI Centre of Excellence, Chitkara University Institute of Engineering and Technology, Chitkara University, 140417 Rajpura, India

[5]Department of Materials Science and Engineering, Cornell University, Ithaca, NY, 14850, USA

[6]Scientific and Technological Research & Application Center, Karamanoglu Mehmetbey University, Karaman, 70100, Turkey

[7]School of Computing and Digital Technology, Faculty of Computing, Engineering and the Built Environment, Birmingham City University, Birmingham B4 7XG, UK

[8]Civil and Environmental Engineering Department, King Fahd University of Petroleum & Minerals, Dhahran 31261, Saudi Arabia

*Corresponding author email: mustafa_kareem97@yahoo.com

+9647719047121

Abstract

Due to enhanced performance, simplicity in manufacturing, scalability, and versatility, lead-halide perovskite-based solar cells (HPSCs) have received much attention in the domains of energy. Lead is presented in nature as a poisonous substance that causes various issues to climate, human health and prevents their further industrialization. Over the past years, there has been a noticeable interest in exploring some alternative lead-free perovskites. However, owing to some intrinsic losses, the performance that may be achieved from these photovoltaics is not up to standards. Thus, for the purpose of efficiency improvement, a comprehensive simulation is required to comprehend the cause of these losses. In the current research, an investigation into how to employ the promisingly efficient lead-free, all-inorganic cesium tin-germanium iodide ($CsSnGeI_3$) perovskites as the photoactive layer in HPSCs. Results exhibited a high efficiency of 12.95% with a $CsSn_{0.5}Ge_{0.5}I_3$ perovskite thickness of 0.6 µm and a bandgap of 1.5 eV at room temperature. High efficiency may be attained by using phenyl-C61-butyric acid methyl ester (PCBM) as an electron transport material because of its favorable energy-level alignment with the perovskite material. The research further

tested the perovskite layer thickness and defect density in depth. The results showed that the carrier diffusion lengths have a big effect on how well the HPSC works.

Keywords: Perovskite solar cells; Simulation; PCBM; Diffusion length

1. Introduction

Since the achievements of 2009 [1], it is widely believed that halide perovskite solar cells (HPSCs) could have a significant effect on the progression of next-generation photovoltaics (PVs) [2-7]. The most efficient HPSCs are based on lead (Pb) perovskites [8-11]. Because Pb is thought to be very dangerous, the fact that it is in these devices has raised some issues, which may slow down or stop the commercialization process [12, 13]. As a backup plan, scientists have been looking for perovskite-like materials that are less toxic. Pb-free materials have received a lot of attention and research, and the first results are promising. However, they have yet to approach the stunning performance of $APbX_3$ semiconductors [14-17]. Pb-free absorbers for photovoltaics should be non-toxic, have narrow energy gaps, high absorption coefficients, high mobilities, high charge-carrier diffusion length, and good stability. Some halides (tin, germanium), a few double perovskites, and Bi/Sb-based halides with perovskite-like phase are only a few examples of the low-toxicity components with perovskite structure that have desirable characteristics [18-22].

In particular, Sn-based perovskite materials have been attracting a lot of interest since they share many of the same features as the other options and have shown the most promise in terms of device performance [23-25]. The direct bandgaps of these perovskites are significantly smaller and more appealing than those of their Pb-based counterparts, ranging from around 1.2 to 1.4 eV [26, 27]. These perovskites exhibit direct bandgaps between 1.2 and 1.4 eV, which are significantly smaller and more desirable than their Pb-based counterparts. Also, the all-inorganic Pb-free cesium tin triiodide ($CsSnI_3$) perovskite is currently the best candidate owing to its enhanced optoelectronic features, making it a potential alternative to Pb-based light absorption perovskites [28, 29]. Substituting Cs for the organic cation in the perovskites has been shown to greatly improve their thermal stability and ambient cell performance [30]. Its power conversion efficiency (PCE) over 10% is the highest of any Pb-free all-inorganic HPSCs [31, 32]. Nevertheless, the easy oxidation of tin(II) to tin(IV) and the accompanying phase instability in the inorganic halide lead to the fast deterioration of its characteristics [33]. Recently, Min and colleagues advocated the addition of germanium (Ge) to $CsSnI_3$ to develop the exceptionally stable and environmentally friendly $CsSnGeI_3$ hybrid perovskite. Thermal evaporation was used to produce all-inorganic $CsSn_{0.5}Ge_{0.5}I_3$ perovskite films with an energy gap of 1.5 eV and a relatively long diffusion length (L_n = 963 nm and L_p = 653 nm), and HPSCs yielded a certified PCE of 7.1%. More remarkably, after 100 hours of continuous light exposure, the $CsSn_{0.5}Ge_{0.5}I_3$ devices still maintain 91% of their original

performance when exposed to ambient air. $CsSnGeI_3$-based HPSC is the most promising light-absorbing semiconductor for use in future Pb-free HPSC applications [34].

Apart from the fabrication, Raghvendra and colleagues reported the modelling perspective of $CsSnGeI_3$-based HPSCs. At an optimized defect density (*Nt*) of 10^{15} cm^{-3} (L_n = 16 µm and L_p = 7.4 µm), the device gave a champion PCE of 10.18% [35]. Another attempt has been made by Neelima and colleagues to enhance the performance of this type of inorganic perovskite. The simulated $CsSnGeI_3$ cell showed best performance with an optimum N_t of 10^{16} cm^{-3} (L_n = 5 µm and L_p = 2.3 µm), achieving a PCE of 20.58% [36]. Sagar and colleagues optimized the Pb-free HPSC with a structure of ITO/titanium oxide (TiO_2)/$CsSn_{0.5}Ge_{0.5}I_3$/Spiro-OMeTAD/Au. The optimized device recorded a PCE of 28.4% by using a low defect density of 10^{14} cm^{-3} (L_n = 50 µm and L_p = 23 µm) [37]. As aforementioned in the above discussion, we believe that the very high efficiency of the simulated $CsSn_{0.5}Ge_{0.5}I_3$ device is because of the overstimulated in the diffusion lengths of photocarriers for the perovskite film, while to the best of our knowledge, the diffusion lengths of the $CsSnI_3$ based perovskite film can only be approached to 1 µm [38]. To predict optimal values for best performance from the photovoltaics, a comprehensive study of the interplay between the many factors that impact $CsSn_{0.5}Ge_{0.5}I_3$ absorbers is required. Preliminary knowledge of the PV may be accessed through modelling. Simulated optimization results will simplify experimental optimization. Herein, a numerical study was carried out employing the Solar Cell Capacitance Simulator-1D (SCAPS-1D). The $CsSnGeI_3$ perovskite has been modelled using this software. The device architecture of F-doped tin oxide (FTO)/PCBM/$CsSnGeI_3$/Spiro-OMeTAD/Au was examined, and the findings were investigated and discussed.

2. Simulation details

For PV modelling, a one-dimensional SCAPS simulation software was employed. The SCPAS program employs Poisson's equation, which defines the relationship between the photocarrier and the semiconductor's electrostatic potential, and continuity equations, which represent charge generation and recombination kinetics in materials [39]. Solving both Poisson's equation and the continuity equation gives us the quantum efficiency (QE) and *J*-*V* properties [40]. Using Poisson's equation and the continuity equation, it is possible to figure out the density of electrons and holes [41, 42]. The distribution of the electric field $E(x)$ can be calculated using Poisson's equation:

$$\frac{dE}{dx} = \frac{\rho}{\varepsilon}, \rho(x) = q(N_D + p - N_A - n)$$

Drift and diffusion current densities control the transportation properties of charge carriers in semiconductor. The following equations describe the drift and diffusion current densities for electrons and holes [22, 39].

$$J_n = qn(x)\mu_n E(x) + qD_n \frac{dn}{dx}$$

$$J_p = qp(x)\mu_p E(x) - qD_p \frac{dp}{dx}$$

Where μ_n and μ_p are to electron hole mobility, respectively, and D_n, and D_p are electron and hole diffusion coefficients respectively. ρ(x), ε, and q refer to space charge distribution, dielectric permittivity, and charge of electron, respectively. n(x) and J_n represent the concentration and current density of electrons. p(x) and J_p represent the concentration and current density of hole.

Seven layers, consisting of perovskite absorber, ETL, HTL, and electrodes, can be constructed into a HPSC using the SCAPS software. All PV computations in this study are performed under AM 1.5G (100 mW/cm^2) conditions. Furthermore, *J-V* parameters at different absorber layer thicknesses, operating temperature, series resistance (R_s), shunt resistance (R_{sh}), and total defect density (Nt) have also been explored. **Table 1** and **Table 2** provide a brief summary of the simulation's most important input parameters. To begin device modelling, we first use UV-vis measurements with to measure the absorbance spectrum and bandgap of the perovskite [43, 44], as shown in **Figure S1**. Then, the $CsSnGeI_3$ spectrum generated by UV-vis is used along with the default absorption spectra of the other layers to perform a full model of the PV device in SCAPS 1D. For the entire analysis, a constant AM 1.5G light spectrum was utilized, and the solar cell's operational temperature was maintained at 300 K for all studies, with the exception of those examining the impact of temperature on HPSC performance. The capture cross sections of an electron and a hole are considered to be 10^{-19} cm^2 for all layers, which are supposed to possess a neutral defect type.

Table 1. Input characteristics of FTO, ETL, $CsSn_{0.5}Ge_{0.5}I_3$, and HTL layers.

Material	**Spiro-OMeTAD**	**$CsSn_{0.5}Ge_{0.5}I_3$**	**PCBM**	**FTO**	**CuI**	**CuSCN**	**Cu_2O**
Thickness (μm)	0.2	0.6 (varied)	0.05	0.2	0.2	0.2	0.2
Bandgap (eV)	2.9	1.5	2	3.2	2.98	3.5	3.5
χ (eV)	2.2	3.9	4	4	2.1	1.8	4.0
ε_r	3	28	3.9	9	6.5	10	7.11
CB effective density of states (1/cm^3)	2.8 x 10^{18}	1 x10^{19}	1.17 x10^{19}	2.2 x10^{18}	10^{22}	10^{22}	2.2 ×10^{18}
VB effective density of states (1/cm^3)	1.8 x10^{19}	1 x10^{19}	1.12 x10^{19}	1.8 x10^{19}	10^{22}	10^{22}	1.8×10^{19}
Electron thermal velocity (cm/s)	1 x10^7	1 x10^7	1 x10^7	1 x10^7	1 x10^7	1 x10^7	1 x10^7
Hole thermal velocity (cm/s)	1 x10^7	1 x10^7	1 x10^7	1 x10^7	1 x10^7	1 x10^7	1 x10^7
μ_e (cm²/Vs)	1 x10^{-4}	974	2 x10^{-2}	20	1.7 ×10^{-4}	1 ×10^{-4}	20
μ_h (cm²/Vs)	1 x10^{-4}	213	2 x10^{-2}	10	1.7 ×10^{-4}	1 ×10^{-4}	10
N_D (1/cm^3)	_	_	1 x10^{16}	2 x10^{19}	-	-	-
N_A (1/cm^3)	1.3 x10^{18}	1 x10^{19}	_	_	2 × 10^{18}	2 × 10^{18}	10^{18}
N_t (1/cm^3)	1 x10^{14}	2.75 x10^{17} (varied)	1 x10^{15}	1 x10^{15}	10^9	10^9	10^{15}

Reference	39	45	46	47	48	49	50

Table 2. Interface parameters of FTO/PCBM/$CsSn_{0.5}Ge_{0.5}I_3$/Spiro-OMeTAD/Au cell.

Interface	**Spiro-OMeTAD/$CsSn_{0.5}Ge_{0.5}I_3$**	**PCBM/$CsSn_{0.5}Ge_{0.5}I_3$**
Defects type	Neutral	Neutral
Capture cross-section for electron (cm^2)	1×10^{-19}	1×10^{-19}
Capture cross-section for hole (cm^2)	1×10^{-19}	1×10^{-19}
Energetic distributions	single	single
Defects energy level Et	up the maximum E_v	up the maximum E_v
Reference for defect energy level Et	0.06	0.06
Total density (integrated over all energies) ($1/cm^2$)	1×10^{10}	1×10^{10}

3. Results and discussion

Figure 1a depicts a schematic of the planar heterojunction structure employed for numerical modelling of HPSC. In this computation, FTO with a work function of 4 eV is considered as the front electrode, PCBM as the ETL, Spiro-OMeTAD as the hole transport layer (HTL), $CsPbSnGeI_3$ composite perovskite is obtained as the light harvester film, and Au as the back electrode. **Figure 1b-c** shows the band diagram for the computed HPSC structure at equilibrium. There is a mismatch of approximately 0.3 eV between the highest occupied molecular orbitals (HOMO) of the HTL and the $CsSnGeI_3$ layer. The mismatch should become low enough for holes to smoothly transit from the perovskite to the HTL [51], as well as a 0.1 eV potential barrier between the lowest unoccupied molecular orbital (LUMO) and the conduction band of the ETL. For optimal HPSC performance, the LUMO of the ETL should be equal to or slightly greater than that of the perovskite material, but this was not the case in the experimental device. Compared to $MASnI_3$-based HPSC, $CsSnGeI_3$-based HPSC exhibits a rapid electron transport rate [37]. **Figure 1d** demonstrates the absorption coefficients of all layers utilized in this simulation work. The perovskite layer has the highest absorbance in the visible range of incident light, which is beneficial for this type of optoelectronic device.

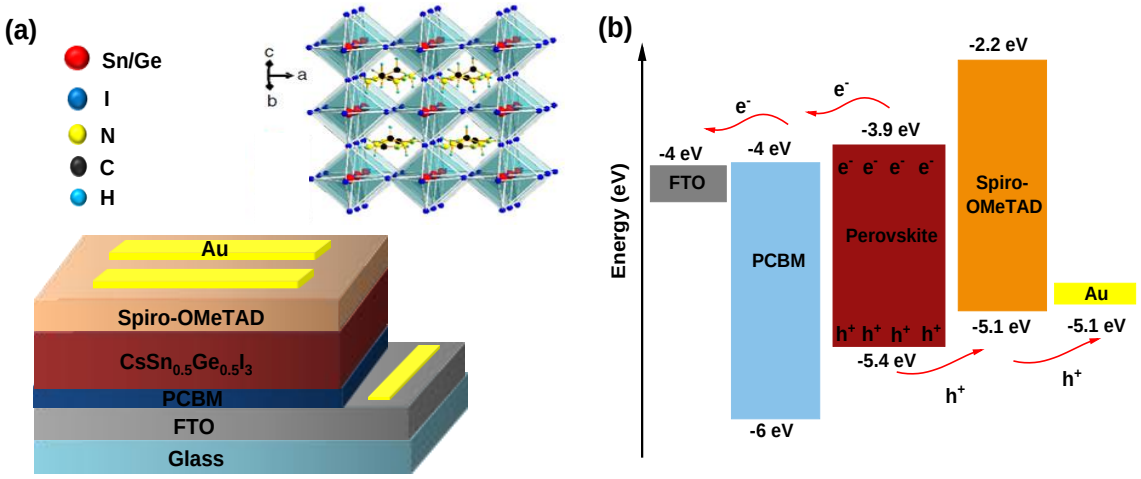

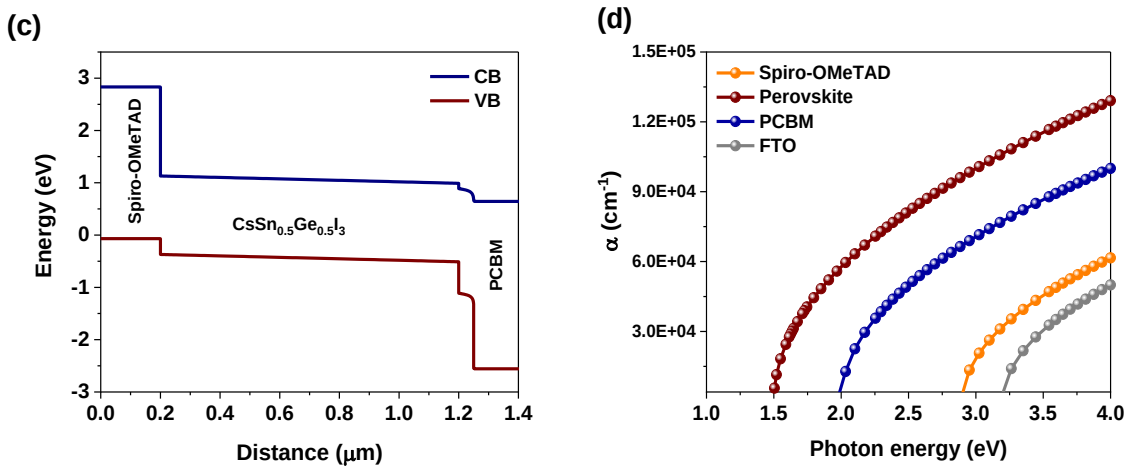

Figure 1. (a) Schematic layout of the HPSC architecture. (b) Schemitic diagram of energy band alingment for $CsSn_{0.5}Ge_{0.5}I_3$ photovoltaic. (c) Energy band diagram of the PSC without illumination. (d) Absorption coefficient of various layers used for simulating HPSCs.

The thickness of the perovskite has a significant role in determining HPSC performance. Therefore, it is essential to optimize perovskite thickness. **Figure 2a** shows how the thickness of the perovskite layer influences the *J-V* plot of the PV device. 0.6 µm is the optimum $CsSnGeI_3$ thickness. Utilizing the same values for all other layers as given in **Table 1**, allows for a variation in $CsSnGeI_3$ thickness of 0.2 µm to 1 µm. With increasing $CsSnGeI_3$ thickness, PCE improves linearly. This is due to the higher rate of absorption, which raises the quantity of photocarriers relative to thickness [52]. However, the PCE reduces when the $CsSnGeI_3$ thickness is increased above the ideal value. The produced electron-hole pairs recombine far above the optimum thickness, which lowers PCE. **Table 3** illustrates the variation of other PV characteristics. V_{OC} decreases with increasing thickness as a result of the increased recombination rates of photocarriers caused by the large production of photocarriers. For a perovskite thickness of 1 µm, the highest value of J_{SC} achieved is 27.008 mA/cm_2. The large absorption coefficient of the absorber layer is responsible for the gradual increment in J_{SC} with respect to thickness [53]. As stated in the literature [40], a rise in resistivity in the device due to an increase in perovskite thickness causes a reduction in FF. The lowest value for FF was roughly 62.07%. Series resistance (*Rs*) gradually rises with increasing perovskite thickness and causes FF to decrease.

Even though several computational analyses claimed that HPSCs using $CsSnGeI_3$ as the perovskite film and PCBM as the ETL performed well [45], experimental research shows that HPSCs using $CsSn_{0.5}Ge_{0.5}I_3$ as the absorber layer had a certified PCE of 7.1% [34]. This shows that the results we achieved by using an accurate DFT absorption spectrum for the $CsSn_{0.5}Ge_{0.5}I_3$ film are in line with the findings of the experiment outputs. Here, additional studies are conducted utilizing the perovskite layer's comparable characteristics by altering the *Rs* and defect density of the absorber film. From **Figure 2b**, we find the HPSCs reveal high QE in the visible range. Hence, devices possess high J_{SC} values. It is evident that a thinner perovskite causes fewer light absorption to occur at longer wavelengths. This is due to less photo-induced carriers being found within the absorber film. Also, at wavelengths longer than

820 nm, there is no light absorption below the bandgaps, so the QE drops to zero. Additionally, QE decreases to zero for wavelengths greater than 820 nm because light cannot be absorbed below the bandgaps. All simulated PV shows a reduction in QE at wavelengths below 390 nm. This is due to photons being mostly captured by the substrate and ETL. Also, we check the influence of the front electrode type on the device performance at an optimized perovskite thickness (0.6 µm). As shown in **Figure S2**, the PCE of HPSC decreased with use of ITO as a front electrode. This reduction is mainly due to the suppression of the FF parameter to 53.16%.

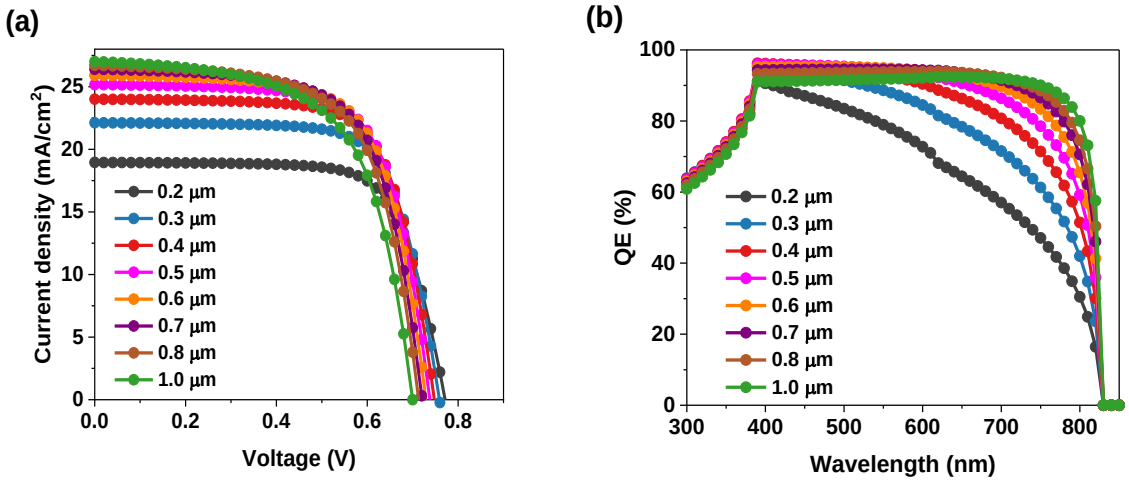

Figure 2. (a) *J-V* characteristics of HPSC devices with variation of absorber layer thickness. (b) The corresponding QE profiles.

Table 3. PV parameters of $CsSn_{0.5}Ge_{0.5}I_3$ cells with variation of perovskite thickness.

Perovskite thickness (µm)	V_{OC} (V)	J_{SC} (mA/cm²)	FF (%)	PCE (%)
0.2	0.771	18.950	71.831	10.504
0.3	0.759	22.120	71.683	12.036
0.4	0.747	24.005	70.969	12.743
0.5	0.738	25.170	69.894	12.985
0.6	0.729	25.912	68.566	12.956
0.7	0.721	26.393	67.065	12.764
0.8	0.713	26.704	65.450	12.472
1.0	0.699	27.008	62.070	11.735

The influence of R_s on PV parameters was investigated, and it was shown to have a crucial role in influencing J_{SC}, FF, V_{OC}, and PCE (**Table S1**). R_s in HPSC has several causes, such as bulk resistance of perovskite, ETL, HTL, interfacial resistance, and the ohmic resistance of the electrodes. As reported, high R_s will decrease the value of PCE, J_{SC}, and V_{OC} of the HPSCs [54]. **Figure 3a** illustrates how J_{SC}, FF, and PCE dropped as *Rs* increased. The V_{OC}, which maintains a constant value of approximately 0.729 V during the whole operation, is unaffected by changes in R_s. This investigation has shown that the performance of the HPSC increases as the R_s decreases. R_s should be decreased in order to improve device performance. It may be accomplished by increasing the cell's ETL, perovskite, and HTL conductivity. The R_s of the device can be decreased by lowering the interface resistance [55].

Photovoltaic performance is severely impacted by low shunt resistance (R_{sh}). R_{sh} reveals perovskite pinholes and recombination processes. **Figure 3b** and **Table S2** illustrate the impact of R_{sh} [56]. This research found that although the value of J_{SC} remained consistent even when the R_{sh} reached 1100 Ω.cm^2, the value of V_{OC} increased slightly with the R_{sh}. Furthermore, the device's FF and PCE steadily rise with R_{sh} value, and the device performance is shown to be constant for a high value of R_{sh} of 1100 Ω.cm^2.

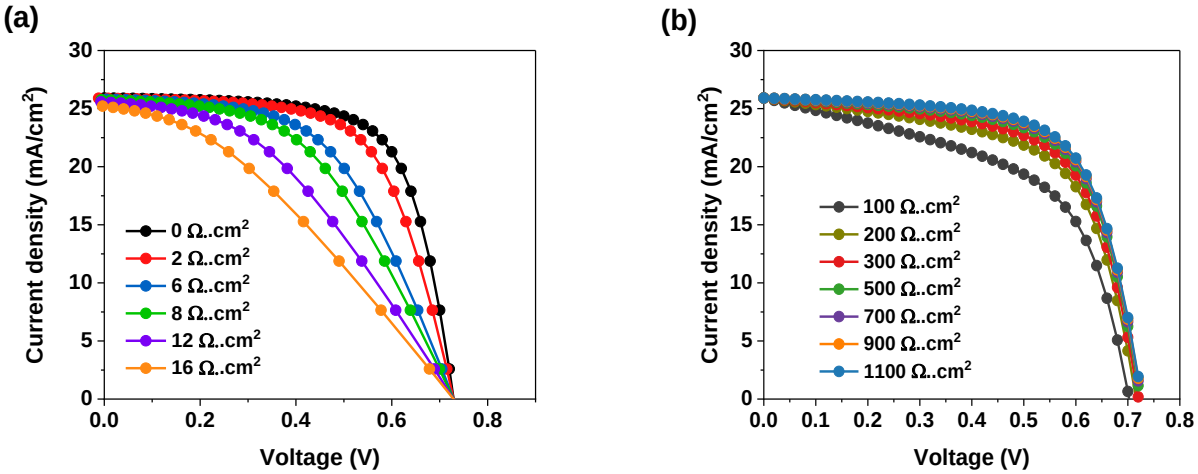

Figure 3. *J-V* characteristics of PSC devices with different (a) series resistances and (b) shunt resistances.

One of the key factors determining HPSC performance is the perovskite defect density (N_t). Numerous defects occupy the perovskite's surface and interior. Nonradiative recombination occurs in the HPSC due to defects in the perovskite that accumulate photogenerated carriers. It has been shown that the density of N_t has a direct relationship to the recombination rate [57]. An increase in N_t causes a rise in charge recombination because the charge carrier lifetime is reduced. *J-V* curves for varying perovskite N_t are described in **Figure 4** and related PV parameters listed in **Table S3**. An increase in perovskite N_t reduces the diffusion length of photocarriers, leading to a high concentration of deep-level defects and a consequently raised rate of non-radiative recombination. The low efficiency of the HPSC is due to the increased recombination rate [58]. Therefore, for higher values of PV parameters,

the N_t of the device should be reduced (**Table 4**), yet devices with a very low N_t are not reported.

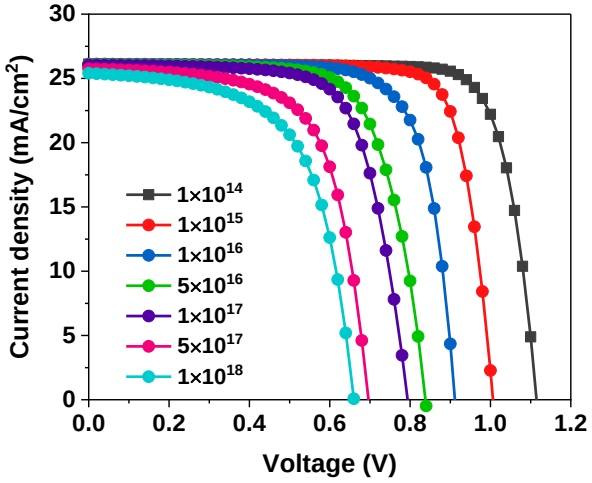

Figure 4. Effect of total defect density on *J-V* characteristics.

Table 4. Influence of N_t and diffusion length of charge carriers on the PSC performance for a constant perovskite thickness of 0.6 µm.

N_t (1/cm³)	L_N (µm)	L_P (µm)	PCE (%)
1×10^{14}	50	23	23.406
1×10^{15}	16	7.4	21.115
1×10^{16}	5	2.3	17.920
5×10^{16}	2.2	1.1	15.591
1×10^{17}	1.6	0.74	14.600
5×10^{17}	0.71	0.33	11.817
1×10^{18}	0.5	0.23	10.310

The photovoltaics are often placed in an outdoor location. The temperature of the cell will rise as a result of the constant exposure to solar radiation, reaching even higher than the ambient temperature. Therefore, it's important to comprehend how device performance characteristics change when the temperature changes. Under continuous lighting, the device's working temperatures vary from 280 K to 350 K. **Figures 5a** and **b** depict the *J-V* plots and PV parameters that vary with respect to the temperature for the $CsSn_{0.5}Ge_{0.5}I_3$-based HPSCs. As the temperature increases from 280 K to 350 K, the V_{OC} of the HPSC-based $CsSnGeI_3$

perovskite film decreases from 0.799 V to 0.588 V, the FF drops from 67.875% to 65.270%, and the PCE decreases from 14.067% to 9.921% (**Table 5**). Nevertheless, J_{SC} was found to be rather consistent at 25.912 mA/cm$_2$. At a higher temperature, the bandgap was narrowed, leading to an increase in photocarrier recombination and a drop in V_{OC}. In addition, an increase in temperature immediately correlates with an increment in defects, reducing V_{OC}. When the temperature rises, HPSC physical characteristics such as charge mobility, as well as the carrier concentration, are influenced by the variation in resistance, resulting in a decline in PCE [36, 59].

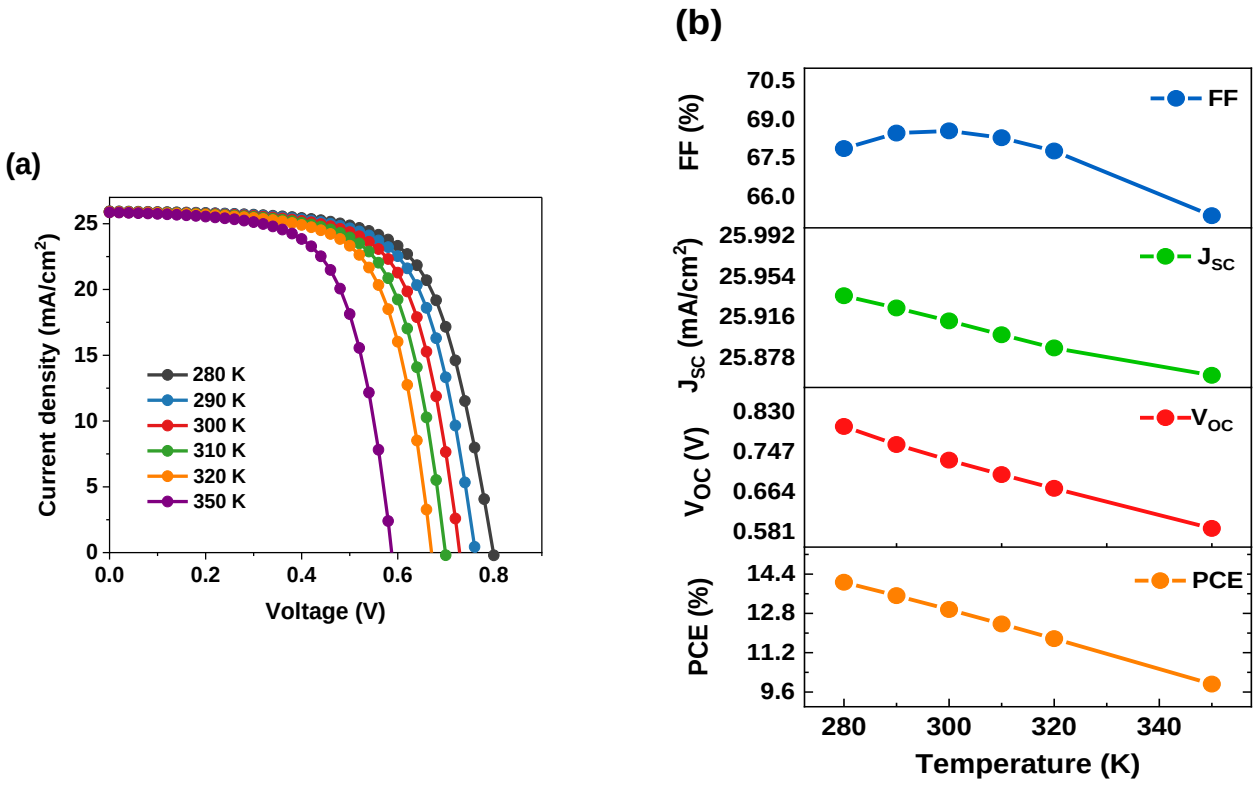

Figure 5. (a) Impact of operating temperature on *J-V* merits. (b) Variation of PV parameters (FF, PCE, V_{OC}, J_{SC})

Table 5. Influence of operating temperature on the PSC performance.

T (°K)	V_{OC} (V)	J_{SC} (mA/cm^2)	FF (%)	PCE (%)
280	0.799	25.936	67.875	14.067
290	0.762	25.925	68.480	13.522
300	0.729	25.912	68.567	12.956
310	0.699	25.899	68.297	12.371
320	0.671	25.887	67.783	11.771

350	0.588	25.861	65.270	9.921

After all else is complete, we get into HTL optimization. To select the optimal hole transport layer (HTL) and establish its PV characteristics, we use inorganic copper iodide (CuI), copper thiocyanate (CuSCN), and copper oxide (Cu_2O) on the HPSC instead of Spiro-OMeTAD. Various *J-V* characteristics for each HTL employed in the HPSC are displayed in **Figure 6**, and their related PV parameters are listed in **Table 6**. Compared to other HTLs, Cu_2O offers superior performance in terms of *J-V* characteristics, J_{SC}, and PCE.

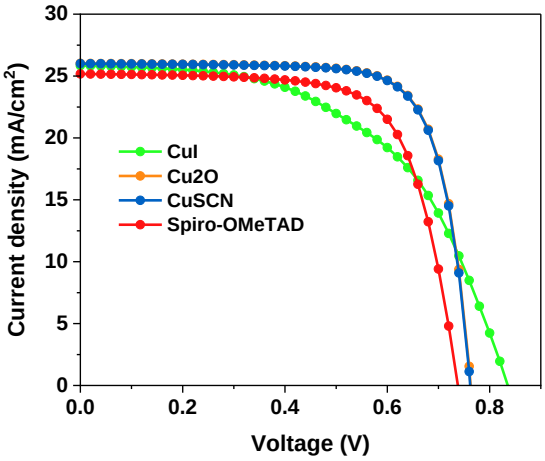

Figure 6. Effect of HTL type on *J-V* plots at an optimized perovskite thickness.

Table 6. *J-V* key parameters of HPSCs using different HTLs.

HTL	V_{OC} (V)	J_{SC} (mA/cm^2)	FF (%)	PCE (%)
Spiro-OMeTAD	0.729	25.91	68.56	12.95
CuSCN	0.762	26.01	75.62	14.98
Cu_2O	0.763	26.02	75.61	15.01
CuI	0.835	25.83	53.43	11.53

4. Conclusions

Using the SCAPS-1D software package, performance tuning studies of HPSCs with inorganic mixed $CsSnGeI_3$ as the photoactive material, PCBM as the ETL, and Spiro-OMeTAD as the HTL show the potential for developing lead-free HPSCs with a decent standard of

performance. The findings suggest that because of the improvement of carrier production and reduced recombination rate, adequate perovskite thickness and low defect density can boost efficiency. The optimized device yielded parameters that correspond to a V_{OC} of 0.729 V, a J_{SC} of 25.912 mA/cm^2, a FF of 68.566%, and a PCE of 12.956%. It is revealed that the PCBM film can replace the common unstable TiO_2 film. For the structure FTO/PCBM/$CsSnGeI_3$/Spiro-OMeTAD/Au, numerical modeling to analyze the influence of different parameters on HPSC efficiency reveals that the ideal thickness and perovskite defect density are 0.6 µm and 1 × 10^{17} cm^{-3}, respectively. The operating temperature of a HPSC has an impact on its efficiency. According to this modeling analysis, 280 K is the ideal operating temperature. Additionally, it has been shown that the device's efficiency suffers when its series resistance exceeds 2 Ω.cm^2. A high shunt resistance value of 1100 Ω.cm^2 is also necessary to achieve optimum HPSC performance.

Conflict of Interest
There is no conflict of interest by any author.

Ethics approval
This article does not contain any studies with human participants or animals performed by the authors.

Consent to participate
We comply with the ethical standards. We provide our consent to take part.

Consent for publication
All the authors are giving consent to publish.

Availability of data and materials
Data will be available based on reasonable request.

Competing interests
Not applicable

Funding
Not applicable

Supporting Information
UV-vis absorption spectrum of perovskite
J-V plots of FTO and ITO-based HPSCs
J-V parameters with respect to series resistance
J-V parameters with respect to shunt resistance
J-V parameters with respect to total defect density

References

1. Kojima, A.; Teshima, K.; Shirai, Y.; Miyasaka, T., Organometal halide perovskites as visible-light sensitizers for photovoltaic cells. *Journal of the american chemical society* **2009,** *131* (17), 6050-6051.
2. Ahmed, D. S.; Mohammed, B. K.; Mohammed, M. K., Long-term stable and hysteresis-free planar perovskite solar cells using green antisolvent strategy. *Journal of Materials Science* **2021,** *56* (27), 15205-15214.
3. Al-Mousoi, A. K.; Mohammed, M. K., Engineered surface properties of MAPI using different antisolvents for hole transport layer-free perovskite solar cell (HTL-free PSC). *Journal of Sol-Gel Science and Technology* **2020,** *96* (3), 659-668.
4. Majeed, S. M.; Ahmed, D. S.; Mohammed, M. K., Anti-solvent engineering via potassium bromide additive for highly efficient and stable perovskite solar cells. *Organic Electronics* **2021,** *99*, 106310.
5. Mohammed, M. K.; Al-Mousoi, A. K.; Mehde, M. S.; Al-Gebori, A. M., Engineered electronic properties of the spin-coated MAPI for hole-transport-free perovskite solar cell (HT-free PSC): Spinning time and PSC performance relationship. *Chemical Physics Letters* **2020,** *754*, 137718.
6. Mohammed, M. K.; Al-Mousoi, A. K.; Singh, S.; Younis, U.; Kumar, A.; Dastan, D.; Ravi, G., Ionic Liquid Passivator for Mesoporous Titanium Dioxide Electron Transport Layer to Enhance the Efficiency and Stability of Hole Conductor-Free Perovskite Solar Cells. *Energy & Fuels* **2022,** *36* (19), 12192-12200.
7. Mohammed, M. K.; Jabir, M. S.; Abdulzahraa, H. G.; Mohammed, S. H.; Al-Azzawi, W. K.; Ahmed, D. S.; Singh, S.; Kumar, A.; Asaithambi, S.; Shekargoftar, M., Introduction of cadmium chloride additive to improve the performance and stability of perovskite solar cells. *RSC advances* **2022,** *12* (32), 20461-20470.
8. Kareem, S. H.; Elewi, M. H.; Naji, A. M.; Ahmed, D. S.; Mohammed, M. K., Efficient and stable pure α-phase FAPbI3 perovskite solar cells with a dual engineering strategy: Additive and dimensional engineering approaches. *Chemical Engineering Journal* **2022,** *443*, 136469.
9. Mohammed, M. K.; K. Al-Mousoi, A.; M. Majeed, S.; Singh, S.; Kumar, A.; Pandey, R.; Madan, J.; Ahmed, D. S.; Dastan, D., Stable Hole-Transporting Material-Free Perovskite Solar Cells with Efficiency Exceeding 14% via the Introduction of a Malonic Acid Additive for a Perovskite Precursor. *Energy & Fuels* **2022** *36* (21) 13187–13194.
10. Mohammed, M. K.; Al-Azzawi, R. K.; Jasim, H. H.; Mohammed, S. H.; Singh, S.; Kadhum, H. H.; Kumar, A.; Sasikumar, P.; Revathy, M.; Jabir, M. S., Adaption of MAPbI3 perovskite with copper phthalocyanine inorganic hole transport layer via nitrosonium tetrafluoroborate additive to enhance performance and stability of perovskite solar cells. *Optical Materials* **2022,** *133*, 112901.
11. Al-Mousoi, A.; Mehde, M.; Al-Gebori, A. In *Annealing temperature effects on the performance of the perovskite solar cells*, IOP Conference Series: Materials Science and Engineering, IOP Publishing: 2020; p 012039.
12. Ke, W.; Kanatzidis, M. G., Prospects for low-toxicity lead-free perovskite solar cells. *Nature communications* **2019,** *10* (1), 1-4.
13. Mehde, M. S.; Al-Gebori, A. M.; Hantoosh, A. K. In *The effect of the spinning speed variation on the perovskite solar cell efficiency*, IOP Conference Series: Materials Science and Engineering, IOP Publishing: 2020; p 012071.
14. Liu, X.; Wu, T.; Luo, X.; Wang, H.; Furue, M.; Bessho, T.; Zhang, Y.; Nakazaki, J.; Segawa, H.; Han, L., Lead-Free Perovskite Solar Cells with Over 10% Efficiency and Size 1 cm2 Enabled by Solvent–Crystallization Regulation in a Two-Step Deposition Method. *ACS Energy Letters* **2021,** *7* (1), 425-431.
15. Meng, X.; Li, Y.; Qu, Y.; Chen, H.; Jiang, N.; Li, M.; Xue, D. J.; Hu, J. S.; Huang, H.; Yang, S., Crystallization Kinetics Modulation of FASnI3 Films with Pre-nucleation Clusters for Efficient Lead-Free Perovskite Solar Cells. *Angewandte Chemie* **2021,** *133* (7), 3737-3742.
16. Wang, S.; Yan, L.; Zhu, W.; Cao, Z.; Zhou, L.; Ding, L.; Hao, F., Suppressing the Formation of Tin Vacancy Yields Efficient Lead-Free Perovskite Solar Cells. *Nano Energy* **2022**, 107416.

17. Akman, E.; Akin, S., Poly (N, N'-bis-4-butylphenyl-N, N'-bisphenyl) benzidine-based interfacial passivation strategy promoting efficiency and operational stability of perovskite solar cells in regular architecture. *Advanced Materials* **2021,** *33* (2), 2006087.
18. Ke, W.; Stoumpos, C. C.; Kanatzidis, M. G., "Unleaded" perovskites: status quo and future prospects of tin-based perovskite solar cells. *Advanced Materials* **2019,** *31* (47), 1803230.
19. Giustino, F.; Snaith, H. J., Toward lead-free perovskite solar cells. *ACS Energy Letters* **2016,** *1* (6), 1233-1240.
20. Sabbah, H., Numerical Simulation of 30% Efficient Lead-Free Perovskite CsSnGeI3-Based Solar Cells. *Materials* **2022,** *15* (9), 3229.
21. Yang, Y.; Liu, C.; Cai, M.; Liao, Y.; Ding, Y.; Ma, S.; Liu, X.; Guli, M.; Dai, S.; Nazeeruddin, M. K., Dimension-controlled growth of antimony-based perovskite-like halides for lead-free and semitransparent photovoltaics. *ACS applied materials & interfaces* **2020,** *12* (14), 17062-17069.
22. Kumar, A.; Singh, S.; Mohammed, M. K., Numerical investigation of single junction environmental friendly double perovskite (Cs2AuBiCl6) solar cell with 20.5% power conversion efficiency and negligible hysteresis. *International Journal of Energy Research* **2022**, *46* (14), 20180-20193.
23. Raja, D. B.; Vidya, R.; Sundaram, K. S., Electronic, structural, and optical properties of Cs2SnGeX6 (X= I, Br, Cl) and mixed halides for solar cell applications. *Solar Energy* **2022,** *245*, 353-364.
24. Hao, F.; Stoumpos, C. C.; Cao, D. H.; Chang, R. P.; Kanatzidis, M. G., Lead-free solid-state organic–inorganic halide perovskite solar cells. *Nature photonics* **2014,** *8* (6), 489-494.
25. Ozturk, T.; Akman, E.; Shalan, A. E.; Akin, S., Composition engineering of operationally stable CsPbI2Br perovskite solar cells with a record efficiency over 17%. *Nano Energy* **2021,** *87*, 106157.
26. Stoumpos, C. C.; Malliakas, C. D.; Kanatzidis, M. G., Semiconducting tin and lead iodide perovskites with organic cations: phase transitions, high mobilities, and near-infrared photoluminescent properties. *Inorganic chemistry* **2013,** *52* (15), 9019-9038.
27. Zhang, W.; Cai, Y.; Liu, H.; Xia, Y.; Cui, J.; Shi, Y.; Chen, R.; Shi, T.; Wang, H. L., Organic-Free and Lead-Free Perovskite Solar Cells with Efficiency over 11%. *Advanced Energy Materials* **2022**, 2202491.
28. Yu, H.; Lu, H.; Xie, F.; Zhou, S.; Zhao, N., Native defect-induced hysteresis behavior in organolead iodide perovskite solar cells. *Advanced Functional Materials* **2016,** *26* (9), 1411-1419.
29. Chung, I.; Lee, B.; He, J.; Chang, R. P.; Kanatzidis, M. G., All-solid-state dye-sensitized solar cells with high efficiency. *Nature* **2012,** *485* (7399), 486-489.
30. Marshall, K.; Walker, M.; Walton, R.; Hatton, R., Enhanced stability and efficiency in hole-transport-layer-free CsSnI3 perovskite photovoltaics. *Nature Energy* **2016,** *1* (12), 1-9.
31. Li, B.; Di, H.; Chang, B.; Yin, R.; Fu, L.; Zhang, Y. N.; Yin, L., Efficient Passivation Strategy on Sn Related Defects for High Performance All-Inorganic CsSnI3 Perovskite Solar Cells. *Advanced Functional Materials* **2021,** *31* (11), 2007447.
32. Ye, T.; Wang, X.; Wang, K.; Ma, S.; Yang, D.; Hou, Y.; Yoon, J.; Wang, K.; Priya, S., Localized electron density engineering for stabilized B-γ CsSnI3-based perovskite solar cells with efficiencies> 10%. *ACS Energy Letters* **2021,** *6* (4), 1480-1489.
33. Chung, I.; Song, J.-H.; Im, J.; Androulakis, J.; Malliakas, C. D.; Li, H.; Freeman, A. J.; Kenney, J. T.; Kanatzidis, M. G., CsSnI3: semiconductor or metal? High electrical conductivity and strong near-infrared photoluminescence from a single material. High hole mobility and phase-transitions. *Journal of the american chemical society* **2012,** *134* (20), 8579-8587.
34. Chen, M.; Ju, M.-G.; Garces, H. F.; Carl, A. D.; Ono, L. K.; Hawash, Z.; Zhang, Y.; Shen, T.; Qi, Y.; Grimm, R. L., Highly stable and efficient all-inorganic lead-free perovskite solar cells with native-oxide passivation. *Nature communications* **2019,** *10* (1), 1-8.
35. Raghvendra, R.; Kumar, R.; Pandey, S., Performance evaluation and material parameter perspective of eco-friendly highly efficient CsSnGeI3 perovskite solar cell. *Superlattices Microstruct.* **2019,** *135*, 106273.

36. Singh, N.; Agarwal, A.; Agarwal, M., Numerical simulation of highly efficient lead-free perovskite layers for the application of all-perovskite multi-junction solar cell. *Superlattices and Microstructures* **2021,** *149*, 106750.
37. Bhattarai, S.; Pandey, R.; Madan, J.; Ahmed, F.; Shabnam, S., Performance improvement approach of all inorganic perovskite solar cell with numerical simulation. *Materials Today Communications* **2022**, 104364.
38. Wu, B.; Zhou, Y.; Xing, G.; Xu, Q.; Garces, H. F.; Solanki, A.; Goh, T. W.; Padture, N. P.; Sum, T. C., Long minority-carrier diffusion length and low surface-recombination velocity in inorganic lead-free CsSnI3 perovskite crystal for solar cells. *Advanced Functional Materials* **2017,** *27* (7), 1604818.
39. Elango, I.; Selvamani, M.; Ramamurthy, P. C.; Kesavan, A. V., Studying VOC in lead free inorganic perovskite photovoltaics by tuning energy bandgap and defect density. *Ceramics International* **2022,** *48* (19), 29414-29420.
40. Jannat, F.; Ahmed, S.; Alim, M. A., Performance analysis of cesium formamidinium lead mixed halide based perovskite solar cell with MoOx as hole transport material via SCAPS-1D. *Optik* **2021,** *228*, 166202.
41. Du, H.-J.; Wang, W.-C.; Zhu, J.-Z., Device simulation of lead-free CH3NH3SnI3 perovskite solar cells with high efficiency. *Chinese Physics B* **2016,** *25* (10), 108802.
42. Kumar, A.; Singh, S.; Mohammed, M. K.; Shalan, A. E., Effect of 2D perovskite layer and multivalent defect on the performance of 3D/2D bilayered perovskite solar cells through computational simulation studies. *Solar Energy* **2021,** *223*, 193-201.
43. Humadi, M. D.; Hussein, H. T.; Mohamed, M. S.; Mohammed, M. K.; Kayahan, E., A facile approach to improve the performance and stability of perovskite solar cells via FA/MA precursor temperature controlling in sequential deposition fabrication. *Optical Materials* **2021,** *112*, 110794.
44. Mohammad, M. R.; Ahmed, D. S.; Mohammed, M. K., ZnO/Ag nanoparticle-decorated single-walled carbon nanotubes (SWCNTs) and their properties. *Surface Review and Letters* **2020,** *27* (03), 1950123.
45. Nalianya, M. A.; Awino, C.; Barasa, H.; Odari, V.; Gaitho, F.; Omogo, B.; Mageto, M., Numerical study of lead free CsSn0. 5Ge0. 5I3 perovskite solar cell by SCAPS-1D. *Optik* **2021,** *248*, 168060.
46. Wang, Y.; Xia, Z.; Liang, J.; Wang, X.; Liu, Y.; Liu, C.; Zhang, S.; Zhou, H., Towards printed perovskite solar cells with cuprous oxide hole transporting layers: a theoretical design. *Semiconductor Science and Technology* **2015,** *30* (5), 054004.
47. Hao, F.; Stoumpos, C. C.; Chang, R. P.; Kanatzidis, M. G., Anomalous band gap behavior in mixed Sn and Pb perovskites enables broadening of absorption spectrum in solar cells. *Journal of the American Chemical Society* **2014,** *136* (22), 8094-8099.
48. Nithya, K.; Sudheer, K., Device modelling of non-fullerene organic solar cell with inorganic CuI hole transport layer using SCAPS 1-D. *Optik* **2020,** *217*, 164790.
49. Madhavan, V. E.; Zimmermann, I.; Baloch, A. A.; Manekkathodi, A.; Belaidi, A.; Tabet, N.; Nazeeruddin, M. K., CuSCN as hole transport material with 3D/2D perovskite solar cells. *ACS Applied Energy Materials* **2019,** *3* (1), 114-121.
50. Lin, L.; Jiang, L.; Li, P.; Fan, B.; Qiu, Y., A modeled perovskite solar cell structure with a Cu2O hole-transporting layer enabling over 20% efficiency by low-cost low-temperature processing. *Journal of Physics and Chemistry of Solids* **2019,** *124*, 205-211.
51. Pitchaiya, S.; Natarajan, M.; Santhanam, A.; Asokan, V.; Yuvapragasam, A.; Ramakrishnan, V. M.; Palanisamy, S. E.; Sundaram, S.; Velauthapillai, D., A review on the classification of organic/inorganic/carbonaceous hole transporting materials for perovskite solar cell application. *Arabian Journal of Chemistry* **2020,** *13* (1), 2526-2557.
52. Jayan K, D.; Sebastian, V., Comparative study on the performance of different Lead-based and Lead-free perovskite solar cells. *Advanced Theory and Simulations* **2021,** *4* (5), 2100027.
53. Patel, P. K., Device simulation of highly efficient eco-friendly CH3NH3SnI3 perovskite solar cell. *Scientific Reports* **2021,** *11* (1), 1-11.

54. Karthick, S.; Velumani, S.; Bouclé, J., Experimental and SCAPS simulated formamidinium perovskite solar cells: A comparison of device performance. *Solar Energy* **2020,** *205*, 349-357.
55. Da, Y.; Xuan, Y.; Li, Q., Quantifying energy losses in planar perovskite solar cells. *Solar Energy Materials and Solar Cells* **2018,** *174*, 206-213.
56. Kesavan, A. V.; Panidhara, K. M.; Ramamurthy, P. C., Role of silver-PC61BM composite electron transport layer in methylammonium lead iodide solar cell. *Materials Letters* **2021,** *302*, 130448.
57. Tian, J.; Xue, Q.; Yao, Q.; Li, N.; Brabec, C. J.; Yip, H. L., Inorganic halide perovskite solar cells: progress and challenges. *Advanced Energy Materials* **2020,** *10* (23), 2000183.
58. Kesavan, A. V.; Rao, A. D.; Ramamurthy, P. C., Tailoring optoelectronic properties of CH3NH3PbI3 perovskite photovoltaics using al nanoparticle modified PC61BM layer. *Solar Energy* **2020,** *201*, 621-627.
59. Schwenzer, J. A.; Rakocevic, L.; Gehlhaar, R.; Abzieher, T.; Gharibzadeh, S.; Moghadamzadeh, S.; Quintilla, A.; Richards, B. S.; Lemmer, U.; Paetzold, U. W., Temperature variation-induced performance decline of perovskite solar cells. *ACS applied materials & interfaces* **2018,** *10* (19), 16390-16399.

TOC